

Single-trial decoding of movement intentions using functional ultrasound neuroimaging

Highlights

- Functional ultrasound (fUS) images motor planning activity in non-human primates
- fUS neuroimaging can predict single-trial movement timing, direction, and effector
- This is a critical step toward less-invasive and scalable brain-machine interfaces

Authors

Sumner L. Norman, David Maresca, Vassilios N. Christopoulos, ..., Mickael Tanter, Mikhail G. Shapiro, Richard A. Andersen

Correspondence

mikhail@caltech.edu (M.G.S.),
richard.andersen@
vis.caltech.edu (R.A.A.)

In brief

Norman et al. use functional ultrasound (fUS) neuroimaging to record brain activity while animals perform motor tasks. They use fUS signals to predict movement timing, direction, and effector (hand or eye). This is a critical step toward brain recording and interface tools that are less invasive, high resolution, and scalable.

Article

Single-trial decoding of movement intentions using functional ultrasound neuroimaging

Sumner L. Norman,^{1,6} David Maresca,^{5,6,7} Vassilios N. Christopoulos,^{1,2,6,8} Whitney S. Griggs,¹ Charlie Demene,^{3,4} Mickael Tanter,^{3,4} Mikhail G. Shapiro,^{5,*} and Richard A. Andersen^{1,2,9,*}

¹Biology & Biological Engineering, California Institute of Technology, Pasadena, CA 91125, USA

²T&C Chen Brain-Machine Interface Center, California Institute of Technology, Pasadena, CA 91125, USA

³Physics for Medicine Paris, INSERM, CNRS, ESPCI Paris, PSL Research University, 75012 Paris, France

⁴INSERM Technology Research Accelerator in Biomedical Ultrasound, Paris, France

⁵Chemistry & Chemical Engineering, California Institute of Technology, Pasadena, CA 91125, USA

⁶These authors contributed equally

⁷Present address: Imaging Physics, TU Delft, 2628 CJ Delft, the Netherlands

⁸Present address: Bioengineering, University of California, Riverside, Riverside, CA, USA

⁹Lead contact

*Correspondence: mikhail@caltech.edu (M.G.S.), richard.andersen@vis.caltech.edu (R.A.A.)

<https://doi.org/10.1016/j.neuron.2021.03.003>

SUMMARY

New technologies are key to understanding the dynamic activity of neural circuits and systems in the brain. Here, we show that a minimally invasive approach based on ultrasound can be used to detect the neural correlates of movement planning, including directions and effectors. While non-human primates (NHPs) performed memory-guided movements, we used functional ultrasound (fUS) neuroimaging to record changes in cerebral blood volume with 100 μm resolution. We recorded from outside the dura above the posterior parietal cortex, a brain area important for spatial perception, multisensory integration, and movement planning. We then used fUS signals from the delay period before movement to decode the animals' intended direction and effector. Single-trial decoding is a prerequisite to brain-machine interfaces, a key application that could benefit from this technology. These results are a critical step in the development of neuro-recording and brain interface tools that are less invasive, high resolution, and scalable.

INTRODUCTION

Novel technologies for interfacing with the brain are key to understanding the dynamic activity of neural circuits and systems and diagnosing and treating neurological diseases. Many neural interfaces are based on intracortical electrophysiology, which provides direct access to the electrical signals of neurons with excellent temporal resolution. However, the electrodes must be implanted via significant-risk open-brain surgery. This process causes acute and chronic local tissue damage (Polikov et al., 2005), and implants suffer material degradation over time (Barrese et al., 2013; Kellis et al., 2019). Invasive electrodes are also difficult to scale and limited in sampling density and brain coverage. These factors limit longevity and performance (Kellis et al., 2019; Welle et al., 2020; Woolley et al., 2013). Noninvasive techniques, such as electroencephalography (EEG) and functional magnetic resonance imaging (fMRI), have achieved considerable success in the research setting. Even so, they are limited by low spatial resolution, summing activity of large brain volumes, and the dispersion of signal through various tissues and bone. Minimally invasive techniques such as epidural electrocorticography (ECoG) span a middle ground, maintaining relatively high performance without damaging healthy brain tissue (Benabid et al., 2019; Shimoda et al., 2012). However, it is

difficult to resolve signals from deep cortical or subcortical structures with spatial specificity. In addition, subdural ECoG remains invasive in requiring penetration of the dura and exposure of underlying brain tissue.

Here, we evaluate the potential of functional ultrasound (fUS) imaging, a recently developed, minimally invasive neuroimaging technique, to provide single-trial decoding of movement intentions, a neural signaling process of fundamental importance and applicability in brain-machine interfaces (BMIs). fUS imaging is a hemodynamic technique that visualizes regional changes in blood volume using ultrafast Doppler angiography (Bercoff et al., 2011; Mace et al., 2013; Macé et al., 2011). It provides excellent spatiotemporal resolution compared to existing functional neuroimaging techniques (<100 μm and 100 ms) and high sensitivity (~1 mm/s velocity; Boido et al., 2019) across a large field of view (several centimeters). Since its introduction in 2011 (Macé et al., 2011), fUS has been used to image neural activity during epileptic seizures (Macé et al., 2011), olfactory stimuli (Osmanski et al., 2014), and behavioral tasks in freely moving rodents (Sieu et al., 2015; Urban et al., 2015). It has also been applied to non-rodent species, including ferrets (Bimbard et al., 2018), pigeons (Rau et al., 2018), non-human primates (NHPs) (Blaize et al., 2020; Dizeux et al., 2019), and humans (Demene et al., 2017; Imbault et al., 2017; Soloukey et al., 2020). Unlike fMRI, fUS can be

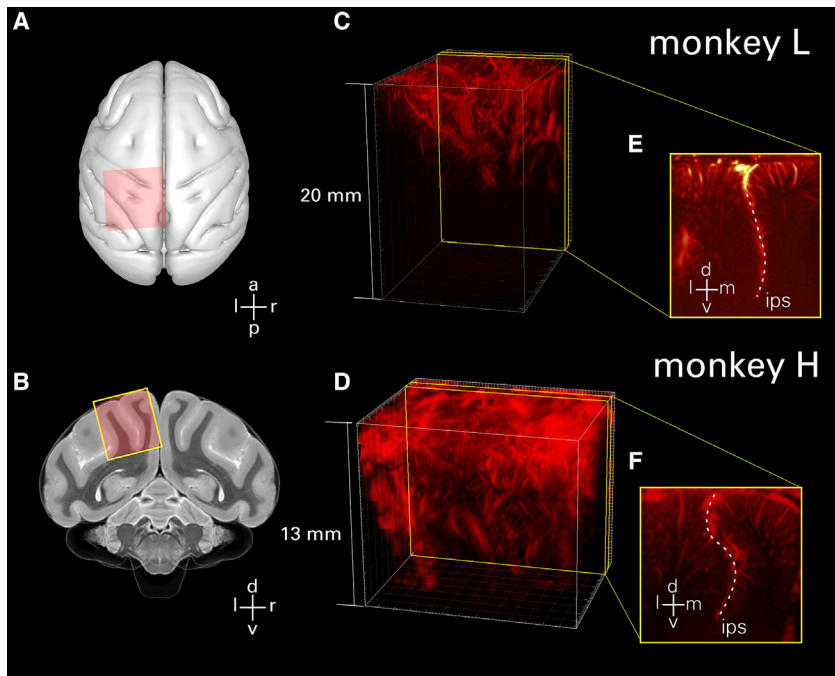


Figure 1. Anatomical scanning regions

(A and B) Illustrations of craniotomy field of view in the axial plane (A) and coronal cross-section (B), overlaid on a NHP brain atlas (Calabrese et al., 2015). The 24 × 24-mm (inner dimension) chambers were placed surface normal to the brain on top of the craniotomized skull.

(C and D) 3D vascular maps for monkey L and monkey H. The field of view included the central and intraparietal sulci for both monkeys.

(E and F) Representative slices for monkey L and monkey H show the intraparietal sulcus (dotted line, labeled *ips*) with orientation markers (l, lateral or left; r, right; m, medial; v, ventral; d, dorsal; a, anterior; p, posterior).

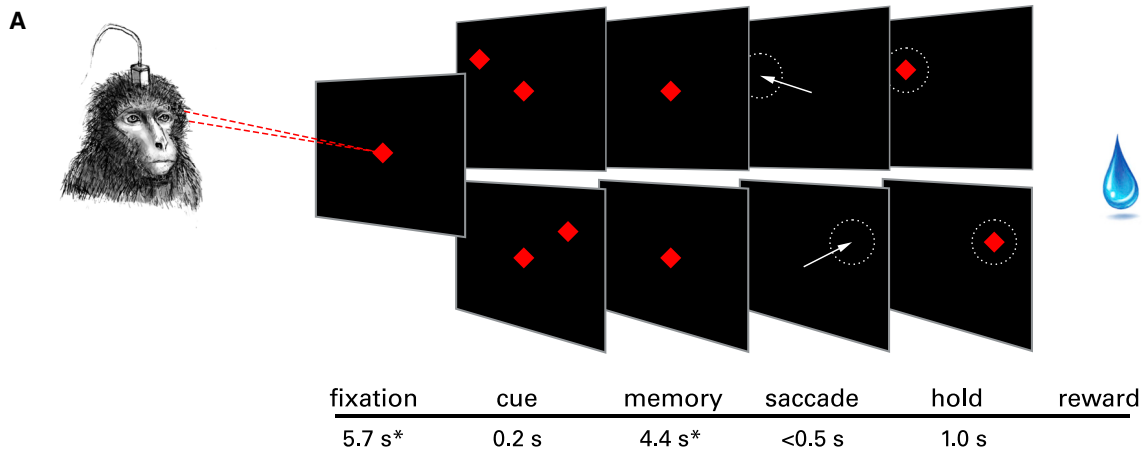
applied in freely moving subjects using miniature, head-mountable transducers (Sieu et al., 2015). In addition, the hemodynamic imaging performance of fUS is ~5- to 10-fold better in terms of spatiotemporal resolution and sensitivity compared to fMRI (Deffieux et al., 2018; Macé et al., 2011; Rabut et al., 2020).

In this study, we leveraged the high sensitivity of fUS imaging to detect movement intentions in NHPs. We trained two animals to perform memory-delayed instructed eye movements (saccades) and hand movements (reaches) to peripheral targets. Meanwhile, we recorded hemodynamic activity over the posterior parietal cortex (PPC) through a cranial window throughout the task. PPC is an association cortical region situated between visual and motor cortical areas and is involved in high-level cognitive functions, including spatial attention (Colby and Goldberg, 1999), multisensory integration (Andersen and Buneo, 2002), and sensorimotor transformations for movement planning (Andersen and Cui, 2009). The functional characteristics of PPC have been thoroughly studied using electrophysiological (Andersen et al., 1987; Andersen and Buneo, 2002; Colby and Goldberg, 1999; Gnadt and Andersen, 1988; Snyder et al., 1997) and functional magnetic resonance techniques (Kagan et al., 2010; Wilke et al., 2012), providing ample evidence for comparison to the fUS data. PPC contains several subregions with anatomical specialization, including the lateral intraparietal area (LIP) involved in planning saccade movements (Andersen et al., 1987; Andersen and Buneo, 2002; Gnadt and Andersen, 1988; Snyder et al., 1997) and the parietal reach region (PRR) involved in planning reach movements (Andersen and Buneo, 2002; Calton et al., 2002; Snyder et al., 2000, 1997). Importantly, their activity can be simultaneously recorded within a single fUS imaging frame (approximate slice volume of 12.8 × 13 × 0.4 mm).

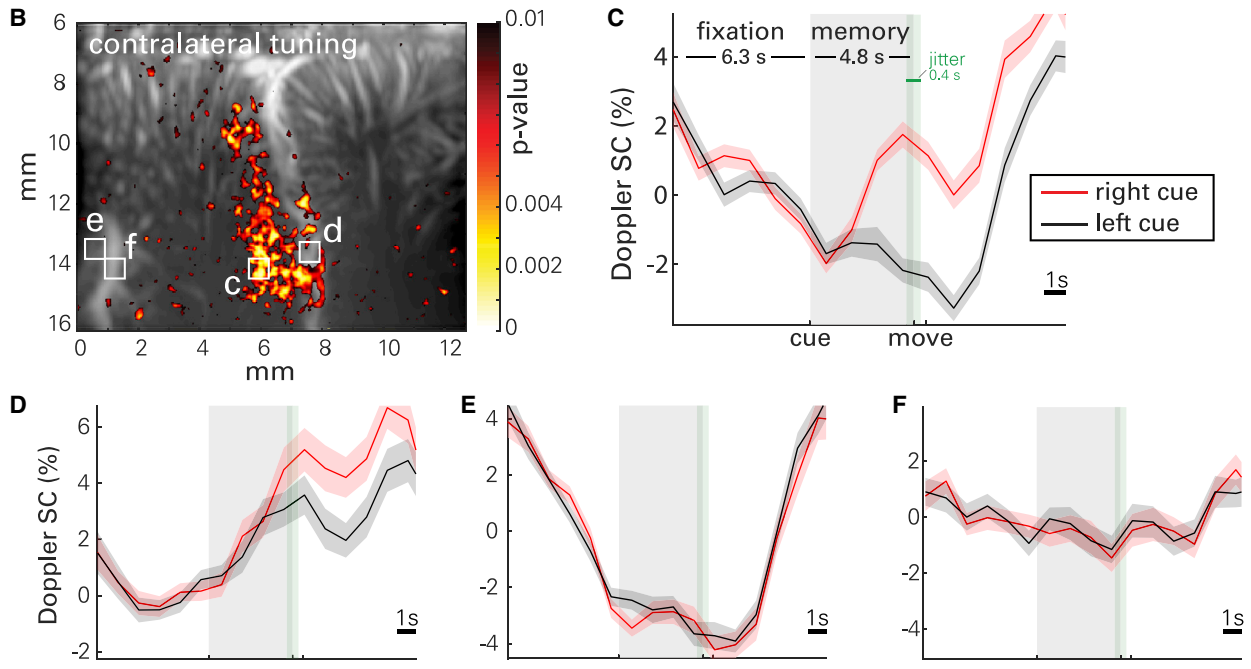
or right). These results show for the first time that fUS is capable of imaging hemodynamics in large animals with enough sensitivity to decode the timing and goals of an intended movement. These findings also represent a critical step toward the use of fUS for BMIs. Such interfaces provide a direct causal link between brain and machine by interpreting neural activity related to user intention. They are excellent tools for neuroscientific investigation (Sakellari et al., 2019) and as a neuroprosthetic to enable people with paralysis to control assistive devices, including computer cursors and prosthetic limbs (Aflalo et al., 2015; Collinger et al., 2013; Hochberg et al., 2012, 2006). As fUS hardware and software developments enable real-time imaging and processing, fUS may prove a valuable tool for future BMIs.

RESULTS

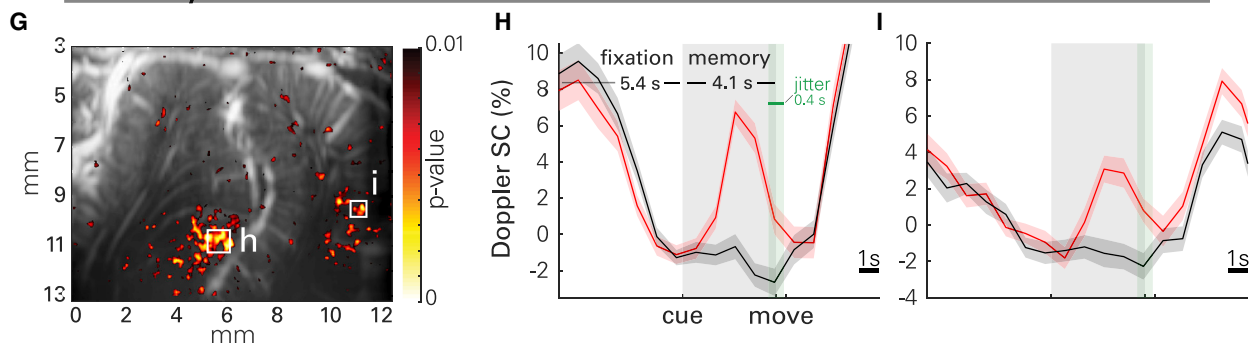
To look for goal-related hemodynamic signals in the PPC, we acquired fUS images from NHPs using a miniaturized 15-MHz, linear array transducer placed on the dura via a cranial window. The transducer provided a spatial resolution of 100 μm × 100 μm in-plane, slice thicknesses of ~400 μm, covering a plane with a width of 12.8 mm and penetration depth of 16 mm. We positioned the probe surface-normal in a coronal orientation above the PPC (Figures 1A and 1B). We then selected planes of interest for each animal from the volumes available (Figures 1C–1F). Specifically, we chose planes that captured both the lateral and medial banks of the intraparietal sulcus (*ips*) within a single image and exhibited behaviorally tuned hemodynamic activity. We used a plane-wave imaging sequence at a pulse repetition frequency of 7,500 Hz and compounded frames collected from a 500-ms period each second to form power Doppler images with a 1 Hz refresh rate.



monkey L



monkey H



(legend on next page)

Hemodynamic response during memory-guided saccades

To resolve goal-specific hemodynamic changes within single trials, we trained two NHPs to perform memory-delayed instructed saccades. We used a similar task design to previous experiments investigating the roles of PPC regions using fMRI blood-oxygen-level-dependent (BOLD) (Kagan et al., 2010; Wilke et al., 2012) and reversible pharmacological inactivation (Christopoulos et al., 2015). Specifically, the monkeys were required to memorize the location of a cue presented in either the left or right hemifield and execute the movement once the center fixation cue extinguished (Figure 2A). The memory phase was chosen to be sufficiently long (from 4.0 to 5.1 s depending on the animals' training and success rate, with a mean of 4.4 s across sessions) to capture hemodynamic changes. We collected fUS data while each animal (N = 2) performed memory-delayed saccades. We collected 2,441 trials over 16 days (1,209 from monkey H and 1,232 from monkey L).

We use statistical parametric maps based on the Student's t test (one sided with false discovery rate [FDR] correction) to visualize patterns of lateralized activity in PPC (Figures 2B and 2G). We observed event-related average (ERA) changes of cerebral blood volume (CBV) throughout the task from localized regions (Figures 2C–2F, 2H, and 2I). Spatial response fields of laterally tuned hemodynamic activity appeared on the lateral bank of *ips* (i.e., in LIP). The response fields and ERA waveforms were similar between animals and are consistent with previous electrophysiological (Graf and Andersen, 2014) and fMRI BOLD (Wilke et al., 2012) results. Specifically, ERAs from LIP show higher memory phase responses to contralateral (right)-compared to ipsilateral (left)-cued trials (one-sided t test of area under the curve during memory phase, t test $p < 0.001$).

Monkey H exhibited a similar direction-tuned response in the presumed medial parietal area (MP), a small patch of cortex on the medial wall of the hemisphere (we did not record this area effect in monkey L, because MP was outside the imaging plane). This tuning supports previous evidence of MP's role in directional eye movement observed in a previous study (Thier and Andersen, 1998). In contrast, focal regions of microvasculature outside the LIP also showed strong event-related responses to the task onset but were not tuned to reach direction (e.g., Figure 2E).

Memory-delayed reaches

In a second experiment, we also collected fUS signals while each NHP performed memory reaches. In total, we collected 1,480 trials (543 from monkey H and 937 from monkey L) over 8 sessions. The task was similar to that of saccades, but the animal's gaze remained fixated throughout the trial, including during the fixation, memory, and reach movement phases (Figure 3A). The memory phase ranged from 3.2 to 5.2 s depending on the animals' training and success rate (mean, 4.2 s across sessions). ERAs on the lateral bank of *ips* reveal populations with direction-specific tuning (Figures 3C, 3D, 3F, and 3G). MP, which was responsive to saccade planning for monkey H (Figure 2I), was not responsive to reach planning. Populations on the medial bank in the putative PRR do not exhibit lateralized tuning but do show bilateral tuning to the movement (Figures 3D and 3G). These results are consistent with electrophysiological recordings, in which the PRR neurons as a population encode both hemispaces, whereas LIP neurons largely encode the contralateral space (Quiñero et al., 2006).

Single-trial decoding

We predicted the direction of upcoming movements using single trials of fUS data (Figure 4A). Briefly, we used class-wise principal-component analysis (CPCA) to reduce data dimensionality. We chose CPCA because it is ideally suited to discrimination problems with high dimension and small sample size (Das and Nenadic, 2009, 2008). We then used ordinary least-squares regression (OLSR) to regress the transformed fUS data (from the memory delay period) to the movement direction (i.e., class label). Finally, we used linear discriminant analysis (LDA) to classify the resulting value for each trial as a presumed left or right movement plan. All reported results were generated using a 10-fold cross-validation. Saccade direction prediction accuracy within a session (i.e., decoded from the memory delay) ranged from 61.5% (binomial test versus chance level, $p = 0.012$) to 100% ($p < 0.001$) on a given 30-min run. The mean accuracy across all sessions and runs was 78.6% ($p < 0.001$). Reach direction prediction accuracy ranged from 73.0% (binomial test versus chance level, $p < 0.001$) to 100% ($p < 0.001$). The mean accuracy across all sessions and runs was 88.5% ($p < 0.001$).

Figure 2. Saccade task, event-related response maps, and waveforms

(A) A trial started with the animals fixating on a central cue (red diamond). Next, a target cue (red diamond) was flashed on either the left or right visual field. During a memory period, the animals had to remember its location while continuing to fixate on the center cue. When the center was extinguished (go signal), the animals performed a saccade to the remembered peripheral target location and maintained eye fixation before receiving a reward. *Mean values across sessions shown; the fixation and memory periods were consistent within each session but varied across sessions from 5.4 to 6.3 s and 4.0 to 5.1 s, respectively, depending on the animals' level of training. The fixation and memory periods were subject to 400 ms of jitter (green shaded area, uniform distribution) to preclude the animal from anticipating the change(s) of the trial phase.

(B–F) Representative activity map and event-related average (ERA) waveforms of CBV change within labeled regions of interest during memory-guided saccades for monkey L.

(B) A statistical map shows localized areas with significantly higher signal change (SC) (one-sided t test of area under the curve, $p < 0.01$) during the memory delay phase for right-cued compared to left-cued saccades, i.e., vascular patches of contralaterally tuned activity.

(C and D) ERA waveforms in LIP display lateralized tuning specific to local populations.

(E) Small vasculature outside of LIP exhibits event-related structure that is tuned to task structure but not target direction.

(F) Vessels that perfuse large areas of cortex do not exhibit event-related signal.

(G–I) Activity map and ERA waveforms within labeled regions of interest for monkey H.

(G) Map for monkey H.

(H) ERA waveforms show lateralized tuning in LIP.

(I) Target tuning also appears in medial parietal area (MP) for monkey H.

(C)–(F) share a common range (9% SC), as do (H) and (I) (14%). ERAs are displayed as means across trials, and shaded areas represent standard error (SEM).

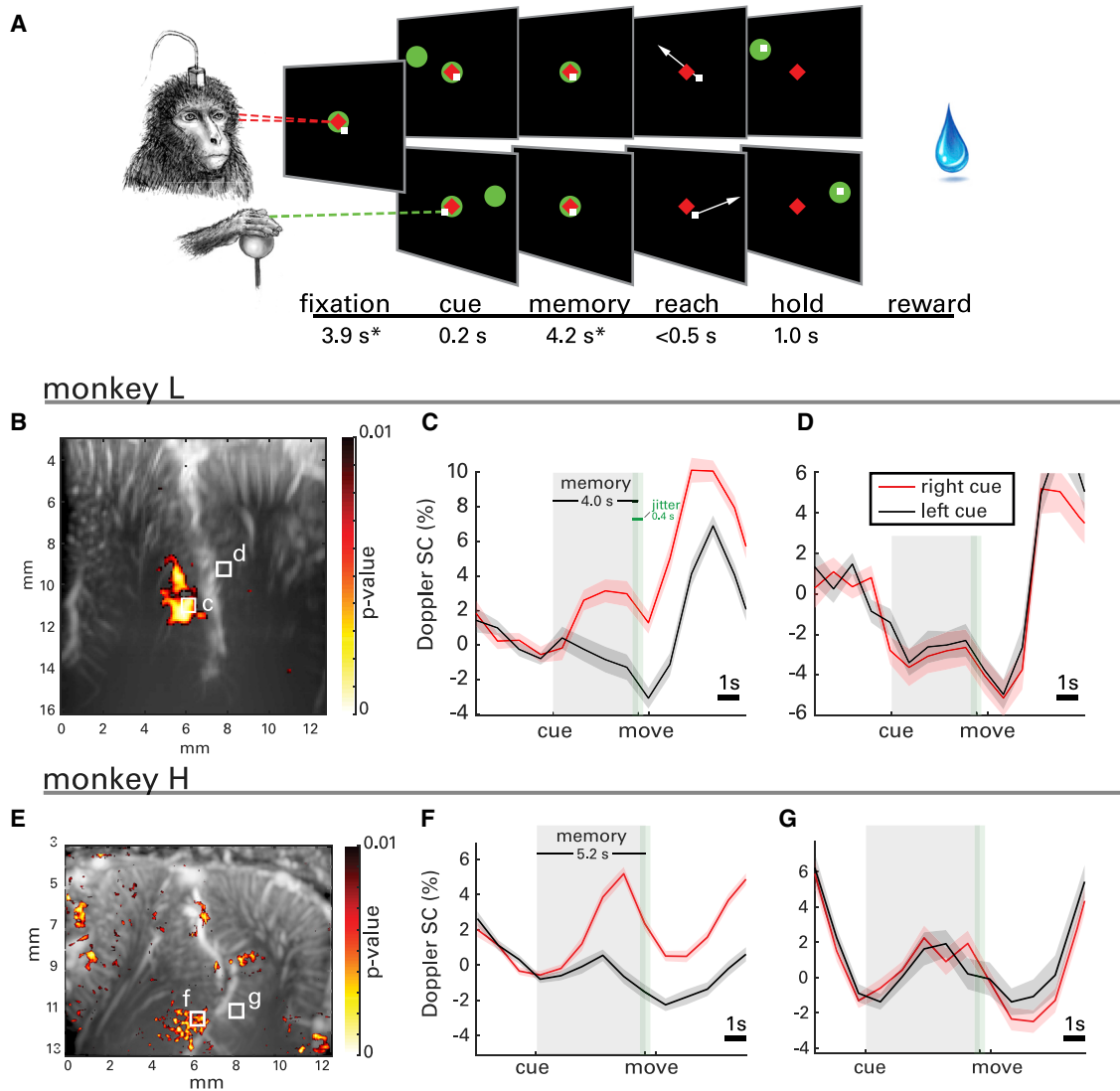


Figure 3. Reach task, event-related response map, and waveforms

(A) Monkeys performed a memory-guided reaching task using a 2D joystick. A trial started with the animal fixating on a central cue (red diamond) and positioning the joystick to its center (green circle). Next, a target (green circle) was flashed on either the left or right visual field. The animal memorized its location while fixating eye and hand on the center cue. When the hand center cue was extinguished (go signal), the animal performed a reach to the remembered target location and maintained the position before receiving a reward. Importantly, eye fixation was maintained throughout the entire trial. *Mean values across sessions shown; the fixation and memory periods were consistent within each session but varied across sessions from 2.5 to 5.9 s and 3.2 to 5.2 s, respectively. The fixation and memory periods were subject to 400 ms of jitter (green shaded area, uniform distribution) to preclude the animal from anticipating the change(s) of the trial phase. (B) A statistical map shows localized areas with significantly higher SC (one-sided t test of area under the curve, $p < 0.01$, false discovery rate [FDR] corrected for number of pixels in image) during the memory delay phase for right-cued compared to left-cued reaches (i.e., vascular patches of contralaterally tuned activity). (C) ERA waveforms from the lateral bank of *ips* reveal lateralized tuning in reaching movements. (D) ERA waveforms in the medial bank of *ips* exhibit a population with bilateral tuning to reaching movements. ERAs are displayed as means across trials, and shaded areas represent standard error (SEM). (E–G) Statistical map and ERA waveforms from monkey H.

To analyze the temporal evolution of direction-specific information in PPC, we attempted to decode the movement direction across time through the trial phases (fixation, memory, and movement). For each time point, we accumulated the preceding data. For example, at $t = 2$ s, we included imaging data from $t = 0$ – 2 s (where $t = 0$ s corresponds to the beginning of fixation). The resulting cross-validated accuracy curves (Figure 4B) show accuracy at

chance level during the fixation phase, increasing discriminability during the memory phase, and sustained decode accuracy during the movement phase. During the memory phase, decoder accuracy improved, surpassing significance 2.08 ± 0.82 s after the monkey received the target cue for saccades (2.32 ± 0.82 s before moving, binomial test versus chance level, $p < 0.05$, Bonferroni corrected for 18 comparisons across time) and 1.92 ± 1.4 s

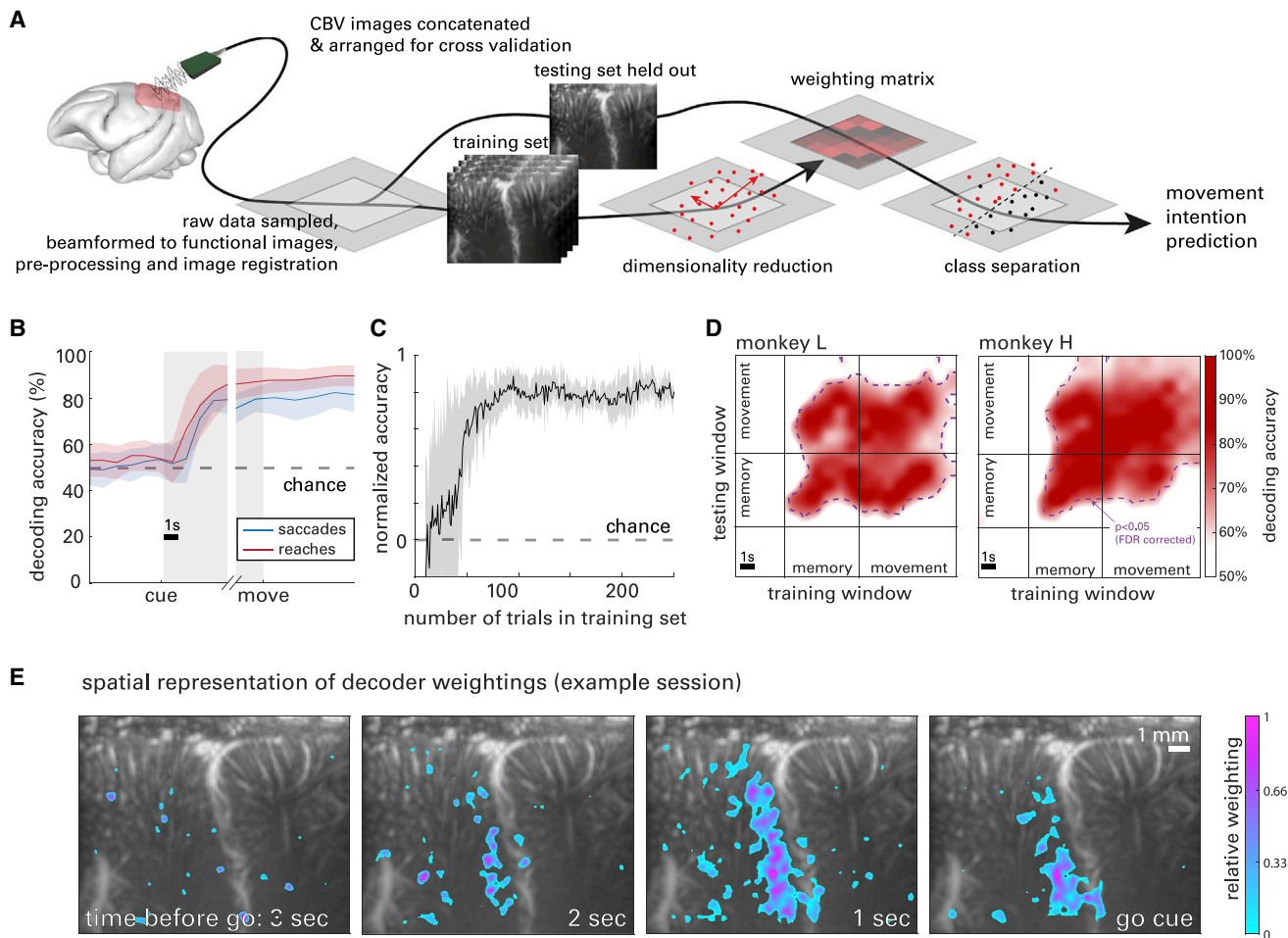


Figure 4. Single-trial decoding of intended movement direction

(A) Data flow chart for cross-validated single-trial movement direction decoding. Training images were separated from testing data according to the cross-validation technique being used. Movement intention predictions were made for single trials based on the dimensionality reduction and a classification model built by the training data with corresponding class labels (i.e., actual movement direction).

(B) Decoding accuracy as a function of time across all datasets.

(C) Decoding accuracy as a function of the number of trials used to train the decoder. Data points in (B) and (C) are means, and shaded areas represent standard error (SEM) across sessions.

(D) Cross-temporal decoder accuracy, using all combinations of training and testing data with a 1-s sliding window. Results are shown in an example session for each animal. Significance threshold is shown as a contour line ($p < 0.05$, FDR corrected). Training the classifiers during the memory or movement phase enabled successful decoding of the memory and movement phases.

(E) Representative decoder weighting maps (monkey L). The top 10% most heavily weighted voxels are shown as a function of space and time before the go cue was given, overlaid on the vascular map.

See also [Figure S1](#) and [Video S1](#).

for reaches (2.28 ± 1.4 s before moving). Decoding accuracy between saccades and reaches was not significantly different.

To determine the amount of data required to achieve maximum decode accuracy, we systematically removed trials from the training set ([Figure 4C](#)). Using just 27 trials, decoder accuracy reached significance for all datasets (binomial test, $p < 0.05$) and continued to increase. Decoder accuracy reached a maximum when given 75 trials of training data, on average.

Were we decoding the neural correlates of positions, trajectories, or goals? To answer this question, we used a cross-temporal decoding technique. We used a 1-s sliding window of data

to train the decoder and then attempted to decode the intended direction from another 1-s sliding window. We repeated this process for all time points through the trial duration, resulting in an $n \times n$ array of accuracies, where n is the number of time windows tested. Cross-validated accuracy was significantly above chance level throughout the memory and movement phases ([Figure 4D](#), purple line, binomial test versus chance level, $p < 0.05$, Bonferroni corrected for 18 time points). In other words, the information we are decoding from this brain region was highly similar during movement preparation and execution. This result suggests that this area is encoding movement plans ([Snyder](#)

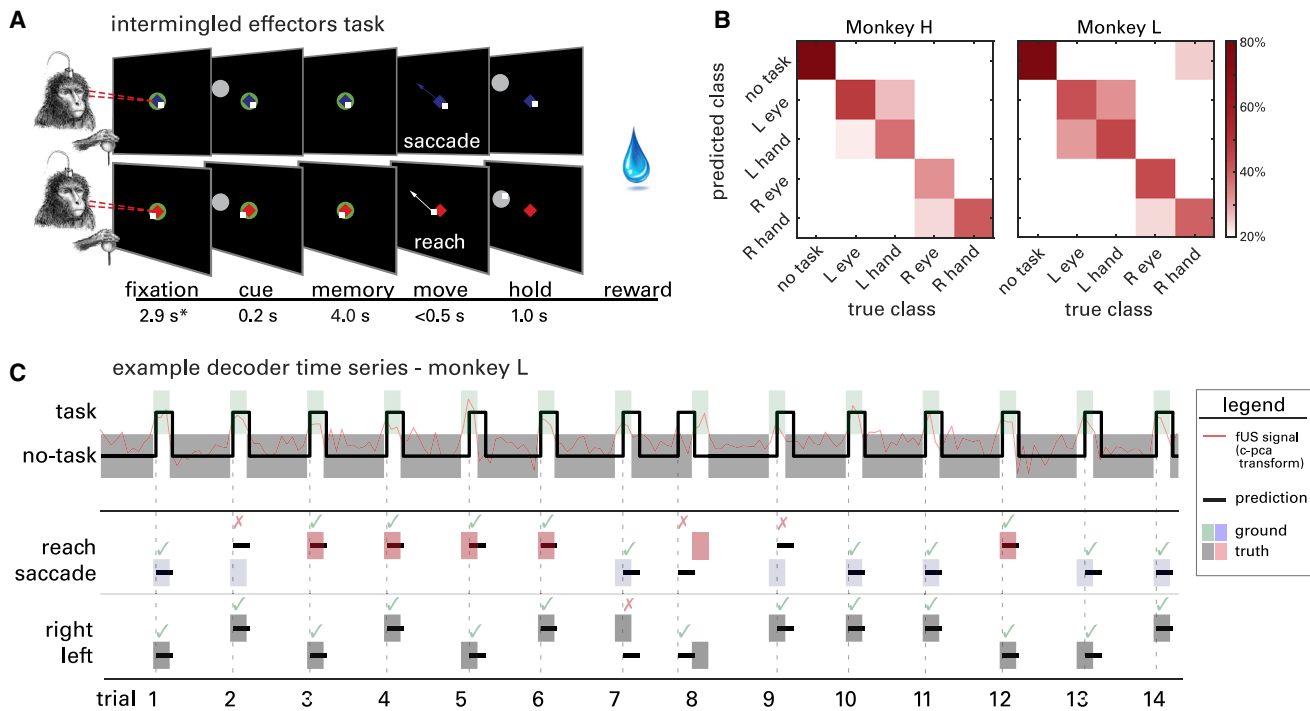


Figure 5. Decoding task, effector, and direction simultaneously

(A) Intermingled memory-delayed saccade and reach task. A trial started with the animals fixating their gaze (and moving the joystick to) a central cue. The center fixation cue was either colored blue to cue saccades (top row) or red to cue reaches (bottom row), randomized trial by trial (i.e., not blocked). Next, a target (white circle) was flashed on either the left or right visual field. The animals had to remember its location while continuing to fixate their eye and hand on the center cue. When the center was extinguished (go signal), the animals performed a movement of either the eye or hand to the remembered peripheral target location. *Mean values across sessions shown; the fixation period was consistent within each session but varied across sessions from 2.4 to 4.3 s.

(B) Confusion matrices of decoding accuracy represented as percentage (columns add to 100%).

(C) Example classification of 14 consecutive trials. Classification predictions are shown as lines, and shaded areas indicate ground truth. An example of the fUS image time series transformed by the classifier subspace appears in red. After predicting the task period, the classifier decoded effector (second row) and movement direction (third row) using data only from the predicted task period (first row).

et al., 1997), visuo-spatial attention (Colby and Goldberg, 1999), or both. Although intention and attention are overlapping abstract concepts that cannot be separated by this experimental design, dissociating their contribution would not fundamentally change our interpretation. Distinct spatial locations within PPC encoded this information, a fact reflected in the variable weighting assigned to each voxel in our decoding algorithm. The decoder placed the highest weightings in area LIP (Figure 4E). This also agrees with the canonical function of this region (Andersen and Buneo, 2002; Gnadt and Andersen, 1988).

Decoding memory period, effector, and direction

To demonstrate the ability of fUS to decode multiple dimensions of behavior from a single trial of data, we trained the same two animals to perform a memory-delayed, intermingled effectors task. This task was similar to the saccade and reach tasks in its temporal structure. However, in addition to the animals fixating their gaze during the fixation period, they also moved a joystick to a central cue with their right hand. This cue's color indicated which effector they should move when the go cue arrived (blue for saccades and red for reaches). If the monkey moved the correct effector (eye/hand) to the correct direction (left/right), then they received a liquid reward (Figure 5A). In total,

we collected 1,576 trials (831 from monkey H and 745 from monkey L) over four sessions (two from each animal) while they performed this task.

We decoded the temporal course of (1) the task structure, (2) the effector, and (3) the target direction of the animal using a decision tree decoder. First, we predicted the task memory periods versus non-memory periods (including movement, inter-trial interval, and fixation). We refer to this distinction as task/no task (Figure 5C, task/no task). To predict when the monkey entered the memory period, the decoder used continuous data where each power Doppler image was labeled as task or no task. After predicting the animal entered the task phase, the second layer of the decision tree used data from the predicted task phase period to classify effector and direction (Figure 5C, reach/saccade, left/right). Each of these decodes used the same strategy as before (cross-validated CPCA). Figure 5B depicts the confusion matrix of decoding accuracy for each class for monkeys H and L. The classifier correctly predicted no-task periods 85.9% and 88.8% of the time for monkeys H and L, respectively, left versus right on 72.8% and 81.5% of trials for monkeys H and L, and eye versus hand on 65.3% and 62.1% of trials for monkeys H and L. All three decodes were significantly above chance level ($p < 0.05$, binomial test versus chance, Bonferroni corrected for three comparisons).

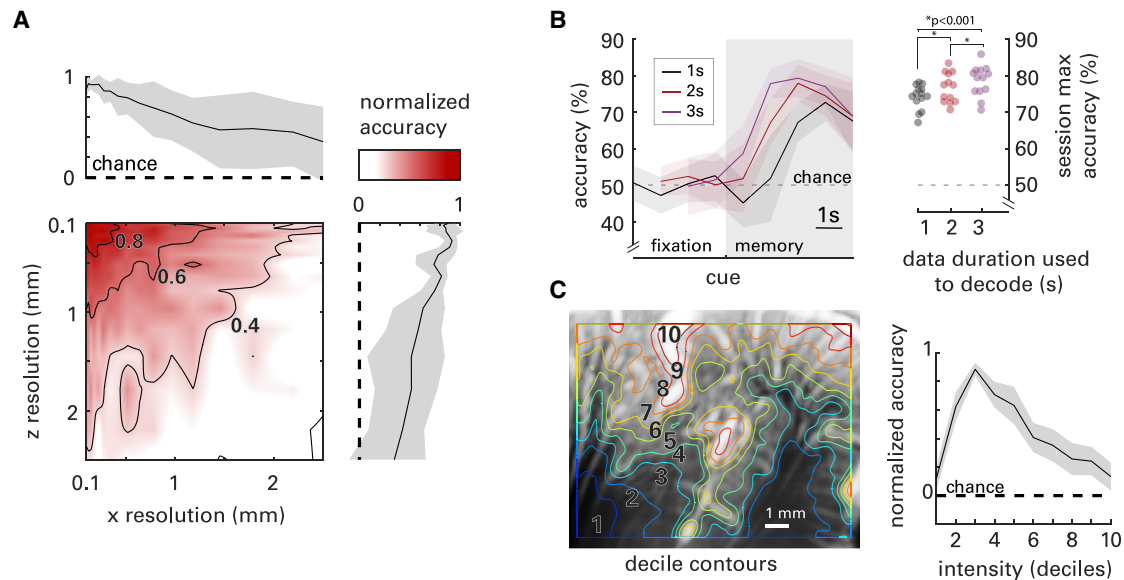


Figure 6. Effects of spatial resolution, time window, and mean power Doppler intensity

(A) Accuracy decreases with resolution in both the x direction (across the imaging plane) and z direction (depth in the plane) in an isotropic manner.

(B) Decoding accuracy as a function of decoder time bin durations (1-, 2-, and 3-s bins represented by black, red, and purple, respectively). Data are aligned to the end of the time bin used for decoding. Dots represent maximum decoder accuracy for each session for each of the bin sizes. Stars indicate statistical significance between groups (Student's t test, $p < 0.001$ for all combinations).

(C) A typical vascular map overlaid with contours dividing the image into deciles of mean power Doppler intensity. Decoding accuracy is shown as a function of the mean power Doppler intensity. Information content is greatest in quantile 3, which mostly contains small vasculature within the cortex. Subcortical and primary unit vasculature (i.e., deciles 1 and 10) are least informative to decoding movement direction.

All data represent means, and shaded areas, when present, represent standard error (SEM) across sessions.

Vascular signal and information content

The purported benefits of fUS compared to established neuroimaging techniques include increased resolution and sensitivity. To test the benefit of increased resolution, we classified movement goals while systematically decreasing the resolution of the image. We resized the images using a low-pass filter in each of the dimensions of the imaging plane, x (across the probe surface) and z (with image depth). We then used the entire image (where the downsized images contained fewer pixels) to decode movement direction. Accuracy continuously decreased as voxel sizes increased (Figure 6A). This effect was isotropic (i.e., similar for both x and z directions).

We hypothesized that functional information useful for decoding would primarily be located in subresolution ($<100 \mu\text{m}$) vessels within the imaging plane. This hypothesis was based on the function of hyperemia, which starts in parenchymal arterioles and first-order capillaries (i.e., vessels of diameter $<50 \mu\text{m}$; Rungta et al., 2018). To test this hypothesis, we ranked voxels by their mean power Doppler intensity and segmented them by deciles, resulting in a spatial map of ranked deciles (Figure 6C). Deciles 1–2 mostly captured subcortical areas. Deciles 3–8 mostly captured cortical layers. Deciles 9 and 10 were largely restricted to large arteries, commonly on the cortical surface and in the sulci. We then classified movement goals using data from each decile. We normalized accuracy for each session, where 0 represents chance level (50%) and 1 represents the maximum accuracy reached across deciles. Accuracy peaked when the regions of the image within the third decile of mean

Doppler power were used to decode movement direction. This decile was mostly represented by cortex vasculature, much of which is at or below the limits of fUS resolution. This result is consistent with our hypothesis that functional hyperemia arises from subresolution vessels (Boido et al., 2019; Maresca et al., 2020) and agrees with previous studies in rodents (Demené et al., 2016) and ferrets (Bimbard et al., 2018).

DISCUSSION

Contributions compared to previous work

This work presents a high-water mark for ultrasound neuroimaging sensitivity that builds on the two previous studies of fUS in NHPs. Significant advances include (1) classification of behavior using fUS data from a single trial, (2) detection of the neural correlates of behavior before its onset, (3) the first investigation of motor planning using fUS, and (4) significant advances in ultrafast ultrasound imaging for single trial and real-time imaging as a precursor to BMI. Dizeux et al. were the first to use fUS in NHPs, finding changes in CBV in the supplementary eye field (SEF) during an eye movement task and mapping directional functional connectivity within cortical layers (Dizeux et al., 2019). Blaize et al. recorded fUS images from the visual cortex (V1, V2, and V3) of NHPs to reconstruct retinotopic maps (Blaize et al., 2020). Both studies explored the boundaries of fUS sensitivity. Dizeux et al. showed that the correlation of fUS signal from SEF and the behavior signal was statistically predictive of the success rate of the animal. However, this prediction required 40 s of data.

Blaize et al. used a binary classification (50% chance level) technique to determine the number of trials necessary to construct retinotopic maps. They reached 89% accuracy after 10 averaged trials for one monkey and 91.8% for the second monkey. Our study is the first to successfully classify fUS activity with just a single trial of data. Furthermore, we predicted the differences between multiple task variables (e.g., effector, direction) in addition to detecting the task itself. We also decoded the behavior of the animal before it was executed. Compared to previous multi-trial detection of a stimulus or task, detecting cognitive state variables from single trials represents a new high bar for fUS neuroimaging. This study represents the first investigation of motor planning and execution using fUS. It thus is the first example in a future body of work using fUS to study the neural correlates of motor learning and motor control in large animals. Finally, the methods developed here are technological achievements by introducing minimal latency (Video S1; Figure S1) and being robust across animals and task paradigms (Figures 2, 3, 4, and 5). Thus, they can be applied in a range of tasks and applications that require real-time signal detection.

Simultaneous effector and direction decoding

PPC's location within the dorsal stream suggests that while visuospatial variables are well represented, other movement variables such as effector may be more difficult to detect. Indeed, decoding accuracy was higher for direction (i.e., left versus right) than for effector (i.e., hand versus eye) (Figure 5B). The observed difference in performance is likely due to PPCs bias toward the contralateral side and partially intermixed populations for effectors in some regions. In addition to direction and effector, we decoded the task versus no-task phases. This is a critical step toward closed-loop feedback environments such as BMI, where the user gates their own movement or the decoder is otherwise not privy to movement or task timing information. Furthermore, simultaneous decoding of task state, direction, and effector is a promising step forward for the use of fUS in both complex behaviors and BMIs.

Comparison of fUS to electrophysiology

There are several clear advantages of fUS monitoring. fUS can reliably record from large portions of the brain simultaneously (e.g., cortical areas LIP and PRR) with a single probe. fUS is also much less invasive than intracortical electrodes; it does not require penetration of the dura mater. This is a significant attribute, because it greatly reduces the risk level of the technique. Furthermore, while tissue reactions degrade the performance of chronic electrodes over time (Woolley et al., 2013), fUS operates epidurally, precluding these reactions. In addition, our approach is highly adaptive thanks to the reconfigurable electronic focusing of the ultrasound beam and its wide field of view. This makes it much easier to target regions of interest. fUS also provides access to cortical areas deep within sulci and subcortical brain structures that are difficult to target with electrophysiology. Finally, the mesoscopic view of neural populations made available by fUS may be favorable for decoder generalization. Thus, training and using decoders across days and/or subjects will be an exciting and important direction of future research.

Other techniques, such as noninvasive scalp EEG, have been used to decode single trials and as a neural basis for control of BMI systems (Norman et al., 2018; Wolpaw et al., 1991; Wolpaw and McFarland, 2004). The earliest proof-of-concept EEG-based BMI achieved a one-bit decode (Nowlis and Kamiya, 1970). Performance of modern EEG BMIs varies greatly across users (Ahn and Jun, 2015) but can yield two degrees of freedom with 70%–90% accuracy (Huang et al., 2009). This performance is comparable to that described here using fUS. However, fUS performance is rapidly increasing as an evolving neuroimaging technique, including recent breakthroughs in 3D fUS neuroimaging (Rabut et al., 2019; Sauvage et al., 2018). These technological advances are likely to herald improvements in fUS single-trial decoding and future BMIs.

Epidural ECoG is a minimally invasive technique used for neuroscientific investigation, clinical diagnostics, and as a recording method for BMIs. Building on the success of more-invasive subdural ECoG, early epidural ECoG in monkeys enabled decoding of continuous 3D hand trajectories with slightly worse accuracy than subdural ECoG (Shimoda et al., 2012). More recently, bilateral epidural ECoG over human somatosensory cortex facilitated decoding of 8 degrees of freedom (4 degrees of freedom per arm, including 3D translation of a robotic arm and wrist flexion) with ~70% accuracy (Benabid et al., 2019). In this study, we demonstrated that unilateral fUS imaging of PPC enabled 3 degrees of freedom with similar accuracy. This is fewer degrees than attainable using modern bilateral ECoG grids. However, it demonstrates that, as a young technique, fUS holds excellent potential. Future work can, for example, extend these findings to similarly record bilateral cortical and subcortical structures, such as M1, PPC, and basal ganglia. As fUS recording technology rapidly advances toward high-speed, wide-coverage, and 3D scanning, these types of recordings will become commonplace.

Advances in fUS technology

Improvements in fUS imaging and computation power continue to accelerate functional frame rates and sensitivity. New scanner prototypes promise faster refresh rates, already reaching 6 Hz (Brunner et al., 2020). Although high temporal resolutions will oversample the hemodynamic response, they enable detection of new feature types (e.g., directional mapping of functional connectivity between brain regions) (Dizeux et al., 2019). The user could also preferentially sacrifice frame rate to compound more frames into functional images, improving image sensitivity. Thus, we anticipate that although these results are a critical step in decoding brain states from a single trial, they are only the first in many forthcoming improvements.

Goal decoding for BMI

The results presented here suggest that fUS has potential as a recording technique for BMI. A potential limitation is the temporal latency of the hemodynamic response to neural activity. Electrophysiology-based BMIs that decode velocity of intended limb movements require as little latency as possible. However, in many cases, goal decoding circumvents the need for instantaneous updates. For example, if a BMI decodes the visuospatial location of a goal (as we do here), then the external effector

(e.g., a robotic arm) can complete the movement without low-level, short-latency information (e.g., joint angles). Furthermore, goal information as found in PPC can represent sequences of consecutive movements (Baldauf et al., 2008) and multiple effectors simultaneously (Chang and Snyder, 2012). Finally, future goal decoders could potentially leverage information from regions in the ventral stream to decode object semantics directly (Bao et al., 2020). These unique advantages of goal decoding could thus improve BMI efficacy without requiring short-latency signals.

fUS BMI in its form in the current study could also enable BMIs outside the motor system. Optimal applications might require access to deep brain structures or large fields of view on time-scales compatible with hemodynamics. For example, cognitive BMIs such as state decoding of mood and other psychiatric states (Shaneshi, 2019) are of great interest due to the astounding prevalence of psychiatric disorders. Like fUS, cognitive BMI is a small but rapidly advancing area of research (Anderesen et al., 2019; Musallam et al., 2004). It is our mission that these areas of research mature together, as they are well matched in timescale and spatial coverage.

One concern about goal decoding is that an error and subsequent change in motor plan happen on short timescales. These sudden changes are difficult to decode regardless of recording methodology, only recently appearing as a potential feature in chronically implanted electrophysiology-based BMIs (Even-Chen et al., 2017). Action inhibition is often attributed to subcortical nuclei, such as the basal ganglia (Jin and Costa, 2010) and subthalamic nucleus (Aron et al., 2016), rather than the cortical areas most often used for BMI. fUS may be able to simultaneously image cortex and these subcortical nuclei but would still be subject to hemodynamic delays. Decreasing system latencies and detecting error signals with complementary methods will be an important topic for future research.

Activity in PPC during saccade planning

Activation maps revealed regions (~100 μm to ~1 cm) within PPC during saccade planning that were more responsive to contralateral targets than ipsilateral targets. Contralateral tuning of these regions during memory delay is consistent with the findings from previous fMRI studies (Kagan et al., 2010; Wilke et al., 2012). Our results are also consistent with the extensive evidence from electrophysiological recordings in NHPs that show LIP is involved in planning and executing saccadic movements (Quiari Quiroga et al., 2006; Snyder et al., 1997). Notably, the ERA waveforms display significantly larger target-specific differences compared to fMRI signals in a memory-delayed saccade task (i.e., 2%–5% versus 0.1%–0.5%) (Kagan et al., 2010; Wilke et al., 2012) and have much finer spatial resolution. This sensitivity was possible despite the deepest subregions of interest extending 16 mm below the probe surface. At this depth, signal attenuation is approximately -7.2 dB (assuming uniform tissue using a 15-MHz probe). Using a probe with a lower center frequency would allow for increasing depths at the cost of spatiotemporal resolution. Use of microbubbles (Errico et al., 2016) or biomolecular contrast agents (Maresca et al., 2020) may enhance hemodynamic contrast, allowing for deeper imaging without sacrificing resolution.

In addition to well-studied PPC subregions, we also identified patches of activity in the MP located within medial parietal area PG (PGm) (Pandya and Seltzer, 1982). These functional areas were much smaller in size and magnitude than those nearer to the *ips*. This may be one potential reason why MP activity was not reported in previous fMRI studies. However, electrophysiological studies have showed that stimulation of this area can elicit goal-directed saccades, indicating its role for eye movements (Thier and Andersen, 1998). The addition of the hemodynamic results presented here is the first hemodynamic evidence of MP function. A limitation of this finding is that we did not observe such activity in the second animal, likely because MP was not in the imaging plane. Current efforts to develop 3D fUS imaging (Rabut et al., 2019) will eliminate this limitation, allowing us to identify new areas based on response properties.

Activity in PPC during reach planning

We also collected data during a memory-delayed reaching task. ERA waveforms identified increases in CBV during the memory phase for regions on the medial aspect of the *ips*. The PRR is located on the medial bank of the *ips* and is characterized by functional selectivity to effector (i.e., the arm) (Christopoulos et al., 2015). The responses we observed in this area were effector specific; they did not appear in the saccadic data. However, they were not direction specific; increases in CBV activity were present for left-cued and right-cued trials. This bilateral reach response can be explained by the spatial scale of the recording method. Whereas single-unit electrophysiology in PRR reveals single neurons that are tuned to contralateral hand movement planning, a significant portion of PRR neurons are also tuned to ipsilateral movement planning (Quiari Quiroga et al., 2006). Within the limits of fUS resolution (~100 μm), each voxel records the hemodynamic response to the summed activity of neurons within the voxel (~100 μm \times 100 μm \times 400 μm). Therefore, our results, in the context of previous literature, provide evidence that (1) populations of ipsilaterally and contralaterally tuned neurons were roughly equivalent, and (2) these populations are mixed at subresolution scales (100 μm). We also found activity on the lateral bank of *ips* that encoded target direction for an upcoming reach. That is, responses were more robust to contralateral targets. Although this area is predominantly involved in saccade movements, neurophysiological studies have also reported neurons within the LIP that encode reaches to peripheral targets (Colby and Duhamel, 1996; Snyder et al., 1997). This area was located more ventral to saccade related areas in the lateral bank of *ips* and may be within the ventral intraparietal area (VIP). VIP is a bimodal visual and tactile area (Duhamel et al., 1998) that produces movements of the body when electrically stimulated (Cooke et al., 2003; Thier and Andersen, 1996), consistent with a possible role in reaching movements.

Instructed versus free movement

We decoded activity as the monkeys performed instructed movements rather than internally driven (“free”) movements. A previous study using fMRI showed that free-choice movements produced similar activation patterns in LIP; however, the difference in signal between left/right targets was smaller than that for instructed movements (Wilke et al., 2012). Given the

improvement in signal made possible with fUS, it may be possible to decode movement direction from single trials of free-choice movements, although accuracy may be impacted. As free-choice movements are more conducive to BMI use, this is an important direction for future research.

Conclusions

The contributions presented here required significant advancements in large-scale recording of hemodynamic activity with single-trial sensitivity. Decoding capabilities are competitive with existing and mature techniques, establishing fUS as a technique for neuroscientific investigation in task paradigms that require single-trial analysis, real-time neurofeedback, or BMI. Although the neurophysiology presented here is in NHPs, we expect that the methods described will transfer well to human neuroimaging, single-trial decoding, and eventually BMI. We first described the visuomotor planning function of PPC using electrophysiology in NHPs (Gnadt and Andersen, 1988; Snyder et al., 1997) and later PPC electrophysiology-based BMI control (Aflalo et al., 2015; Sakellaridi et al., 2019). Translation of these findings into human neuroimaging and BMI is an important direction of future study. In addition to its utility for neuroscientific investigation, brain-machine interfacing is a promising technique to restore movement to people living with neurological injury and disease. The advancements presented here are a critical first step in ushering in a new era of BMIs that are less-invasive, high-resolution, and scalable. These tools will empower researchers to make unique insights into the function and malfunction of brain circuits, including neurological injury and disease. Furthermore, future work advancing these findings could make a large impact in neuroprosthetics by developing and disseminating high-performance, minimally invasive BMIs.

STAR★METHODS

Detailed methods are provided in the online version of this paper and include the following:

- **KEY RESOURCES TABLE**
- **RESOURCE AVAILABILITY**
 - Lead contact
 - Materials availability
 - Data and code availability
- **EXPERIMENTAL MODEL AND SUBJECT DETAILS**
- **METHOD DETAILS**
 - Animal preparation and implant
 - Behavioral setup
 - Behavioral tasks
 - Functional ultrasound sequence and recording
 - Power Doppler image processing
- **QUANTIFICATION AND STATISTICAL ANALYSIS**
 - ERA waveforms and statistical parametric maps
 - Single trial decoding
 - Analysis of training set sample size
 - Multicoder for intermingled effectors task
 - Cross temporal decoding
 - Decoding with reduced spatial resolution
 - Decoding with different time windows
 - Power Doppler quantiles

SUPPLEMENTAL INFORMATION

Supplemental information can be found online at <https://doi.org/10.1016/j.neuron.2021.03.003>.

ACKNOWLEDGMENTS

We thank Kelsie Pejsa for assistance with animal care, surgeries, and training. We thank Thomas Deffieux for his contributions to the ultrasound neuroimaging methods that made this work possible. We thank Igor Kagan for assisting in implantation planning. We thank Charles Liu and Claire Rabut for helpful discussions. Finally, we thank Krissta Passanante for her illustrations. S.N. was supported by a Della Martin Postdoctoral Fellowship. D.M. was supported by a Human Frontiers Science Program Cross-Disciplinary Postdoctoral Fellowship (award LT000637/2016). W.G. was supported by the UCLA-Caltech MSTP (NIGMS T32 GM008042). This research was supported by the National Institute of Health BRAIN Initiative (grant U01NS099724 to M.G.S.), the T&C Chen Brain-machine Interface Center, and the Boswell Foundation (R.A.A.). Related research in the Shapiro lab is supported by the Heritage Medical Research Institute.

AUTHOR CONTRIBUTIONS

S.L.N., D.M., V.N.C., M.T., M.G.S., and R.A.A. conceived the study; D.M. and C.D. established the imaging sequences; S.L.N., V.N.C., and W.G. trained the animals; S.L.N., V.N.C., D.M., and W.G. acquired the data; S.L.N., D.M., and V.N.C. performed the data processing; S.L.N., D.M., and V.N.C. drafted the manuscript with substantial contribution from M.G.S. and R.A.A., and all authors edited and approved the final version of the manuscript; M.T., M.G.S., and R.A.A. supervised the research.

DECLARATION OF INTERESTS

M.T. is a co-founder and shareholder of Iconeus Company, which commercializes ultrasonic neuroimaging scanners. D.M. is now affiliated with T.U. Delft, Netherlands. V.C. is now affiliated with University of California, Riverside.

Received: July 2, 2020

Revised: December 29, 2020

Accepted: March 1, 2021

Published: March 22, 2021

REFERENCES

- Aflalo, T., Kellis, S., Klaes, C., Lee, B., Shi, Y., Pejsa, K., Shanfield, K., Hayes-Jackson, S., Aisen, M., Heck, C., et al. (2015). Neurophysiology. Decoding motor imagery from the posterior parietal cortex of a tetraplegic human. *Science* 348, 906–910.
- Ahn, M., and Jun, S.C. (2015). Performance variation in motor imagery brain-computer interface: a brief review. *J. Neurosci. Methods* 243, 103–110.
- Andersen, R.A., and Buneo, C.A. (2002). Intentional maps in posterior parietal cortex. *Annu. Rev. Neurosci.* 25, 189–220.
- Andersen, R.A., and Cui, H. (2009). Intention, action planning, and decision making in parietal-frontal circuits. *Neuron* 63, 568–583.
- Andersen, R.A., Essick, G.K., and Siegel, R.M. (1987). Neurons of area 7 activated by both visual stimuli and oculomotor behavior. *Exp. Brain Res.* 67, 316–322.
- Andersen, R.A., Aflalo, T., and Kellis, S. (2019). From thought to action: The brain-machine interface in posterior parietal cortex. *Proc. Natl. Acad. Sci. USA* 116, 26274–26279.
- Aron, A.R., Herz, D.M., Brown, P., Forstmann, B.U., and Zablouk, K. (2016). Frontosubthalamic circuits for control of action and cognition. *J. Neurosci.* 36, 11489–11495.
- Baldauf, D., Cui, H., and Andersen, R.A. (2008). The posterior parietal cortex encodes in parallel both goals for double-reach sequences. *J. Neurosci.* 28, 10081–10089.

- Bao, P., She, L., McGill, M., and Tsao, D.Y. (2020). A map of object space in primate inferotemporal cortex. *Nature* 583, 103–108.
- Barrese, J.C., Rao, N., Paroo, K., Triebwasser, C., Vargas-Irwin, C., Franquemont, L., and Donoghue, J.P. (2013). Failure mode analysis of silicon-based intracortical microelectrode arrays in non-human primates. *J. Neural Eng.* 10, 066014.
- Benabid, A.L., Costecalde, T., Eliseyev, A., Charvet, G., Verney, A., Karakas, S., Foerster, M., Lambert, A., Morinière, B., Abroug, N., et al. (2019). An exoskeleton controlled by an epidural wireless brain-machine interface in a tetraplegic patient: a proof-of-concept demonstration. *Lancet Neurol.* 18, 1112–1122.
- Bercoff, J., Montaldo, G., Loupas, T., Savery, D., Mézière, F., Fink, M., and Tanter, M. (2011). Ultrafast compound Doppler imaging: providing full blood flow characterization. *IEEE Trans. Ultrason. Ferroelectr. Freq. Control* 58, 134–147.
- Bimbard, C., Demene, C., Girard, C., Radtke-Schuller, S., Shamma, S., Tanter, M., and Boubenec, Y. (2018). Multi-scale mapping along the auditory hierarchy using high-resolution functional UltraSound in the awake ferret. *eLife* 7, e35028.
- Blaize, K., Arcizet, F., Gesnik, M., Ahnine, H., Ferrari, U., Deffieux, T., Pouget, P., Chavane, F., Fink, M., Sahel, J.-A., et al. (2020). Functional ultrasound imaging of deep visual cortex in awake nonhuman primates. *Proc. Natl. Acad. Sci. USA* 117, 14453–14463.
- Boido, D., Rungta, R.L., Osmanski, B.-F., Roche, M., Tsurugizawa, T., Le Bihan, D., Ciobanu, L., and Charpak, S. (2019). Mesoscopic and microscopic imaging of sensory responses in the same animal. *Nat. Commun.* 10, 1110.
- Brunner, C., Grillet, M., Sans-Dublanc, A., Farrow, K., Lambert, T., Macé, E., Montaldo, G., and Urban, A. (2020). A Platform for Brain-wide Volumetric Functional Ultrasound Imaging and Analysis of Circuit Dynamics in Awake Mice. *Neuron* 108, 861–875.e7.
- Calabrese, E., Badea, A., Coe, C.L., Lubach, G.R., Shi, Y., Styner, M.A., and Johnson, G.A. (2015). A diffusion tensor MRI atlas of the postmortem rhesus macaque brain. *Neuroimage* 117, 408–416.
- Calton, J.L., Dickinson, A.R., and Snyder, L.H. (2002). Non-spatial, motor-specific activation in posterior parietal cortex. *Nat. Neurosci.* 5, 580–588.
- Chang, S.W.C., and Snyder, L.H. (2012). The representations of reach endpoints in posterior parietal cortex depend on which hand does the reaching. *J. Neurophysiol.* 107, 2352–2365.
- Christopoulos, V.N., Bonaiuto, J., Kagan, I., and Andersen, R.A. (2015). Inactivation of parietal reach region affects reaching but not saccade choices in internally guided decisions. *J. Neurosci.* 35, 11719–11728.
- Colby, C.L., and Duhamel, J.-R. (1996). Spatial representations for action in parietal cortex. *Brain Res. Cogn. Brain Res.* 5, 105–115.
- Colby, C.L., and Goldberg, M.E. (1999). Space and attention in parietal cortex. *Annu. Rev. Neurosci.* 22, 319–349.
- Collinger, J.L., Wodlinger, B., Downey, J.E., Wang, W., Tyler-Kabara, E.C., Weber, D.J., McMorland, A.J., Velliste, M., Boninger, M.L., and Schwartz, A.B. (2013). High-performance neuroprosthetic control by an individual with tetraplegia. *Lancet* 381, 557–564.
- Cooke, D.F., Taylor, C.S., Moore, T., and Graziano, M.S. (2003). Complex movements evoked by microstimulation of the ventral intraparietal area. *Proc. Natl. Acad. Sci. USA* 100, 6163–6168.
- Das, K., and Nenadic, Z. (2008). Approximate information discriminant analysis: A computationally simple heteroscedastic feature extraction technique. *Pattern Recognit.* 41, 1548–1557.
- Das, K., and Nenadic, Z. (2009). An efficient discriminant-based solution for small sample size problem. *Pattern Recognit.* 42, 857–866.
- Deffieux, T., Demene, C., Pernot, M., and Tanter, M. (2018). Functional ultrasound neuroimaging: a review of the preclinical and clinical state of the art. *Curr. Opin. Neurobiol.* 50, 128–135.
- Demene, C., Deffieux, T., Pernot, M., Osmanski, B.-F., Biran, V., Gennisson, J.-L., Sieu, L.-A., Bergel, A., Franqui, S., Correas, J.-M., et al. (2015). Spatiotemporal clutter filtering of ultrafast ultrasound data highly increases Doppler and fUltrasound sensitivity. *IEEE Trans. Med. Imaging* 34, 2271–2285.
- Demene, C., Tiran, E., Sieu, L.-A., Bergel, A., Gennisson, J.L., Pernot, M., Deffieux, T., Cohen, I., and Tanter, M. (2016). 4D microvascular imaging based on ultrafast Doppler tomography. *Neuroimage* 127, 472–483.
- Demene, C., Baranger, J., Bernal, M., Delanoe, C., Auvin, S., Biran, V., Alison, M., Mairesse, J., Harribaud, E., Pernot, M., et al. (2017). Functional ultrasound imaging of brain activity in human newborns. *Sci. Transl. Med.* 9, eaah6756.
- Dizeux, A., Gesnik, M., Ahnine, H., Blaize, K., Arcizet, F., Picaud, S., Sahel, J.-A., Deffieux, T., Pouget, P., and Tanter, M. (2019). Functional ultrasound imaging of the brain reveals propagation of task-related brain activity in behaving primates. *Nat. Commun.* 10, 1400.
- Do, A.H., Wang, P.T., King, C.E., Abiri, A., and Nenadic, Z. (2011). Brain-computer interface controlled functional electrical stimulation system for ankle movement. *J. Neuroeng. Rehabil.* 8, 49.
- Do, A.H., Wang, P.T., King, C.E., Chun, S.N., and Nenadic, Z. (2013). Brain-computer interface controlled robotic gait orthosis. *J. Neuroeng. Rehabil.* 10, 111.
- Duhamel, J.-R., Colby, C.L., and Goldberg, M.E. (1998). Ventral intraparietal area of the macaque: congruent visual and somatic response properties. *J. Neurophysiol.* 79, 126–136.
- Errico, C., Osmanski, B.-F., Pezet, S., Couture, O., Lenkei, Z., and Tanter, M. (2016). Transcranial functional ultrasound imaging of the brain using microbubble-enhanced ultrasensitive Doppler. *Neuroimage* 124 (Pt A), 752–761.
- Even-Chen, N., Stavisky, S.D., Kao, J.C., Ryu, S.I., and Shenoy, K.V. (2017). Augmenting intracortical brain-machine interface with neurally driven error detectors. *J. Neural Eng.* 14, 066007.
- Gnadt, J.W., and Andersen, R.A. (1988). Memory related motor planning activity in posterior parietal cortex of macaque. *Exp. Brain Res.* 70, 216–220.
- Graf, A.B., and Andersen, R.A. (2014). Brain-machine interface for eye movements. *Proc. Natl. Acad. Sci. USA* 111, 17630–17635.
- Hochberg, L.R., Serruya, M.D., Friehs, G.M., Mukand, J.A., Saleh, M., Caplan, A.H., Branner, A., Chen, D., Penn, R.D., and Donoghue, J.P. (2006). Neuronal ensemble control of prosthetic devices by a human with tetraplegia. *Nature* 442, 164–171.
- Hochberg, L.R., Bacher, D., Jarosiewicz, B., Masse, N.Y., Simeral, J.D., Vogel, J., Haddadin, S., Liu, J., Cash, S.S., van der Smagt, P., and Donoghue, J.P. (2012). Reach and grasp by people with tetraplegia using a neurally controlled robotic arm. *Nature* 485, 372–375.
- Huang, D., Lin, P., Fei, D.-Y., Chen, X., and Bai, O. (2009). Decoding human motor activity from EEG single trials for a discrete two-dimensional cursor control. *J. Neural Eng.* 6, 046005.
- Imbault, M., Chauvet, D., Gennisson, J.-L., Capelle, L., and Tanter, M. (2017). Intraoperative functional ultrasound imaging of human brain activity. *Sci. Rep.* 7, 7304.
- Jin, X., and Costa, R.M. (2010). Start/stop signals emerge in nigrostriatal circuits during sequence learning. *Nature* 466, 457–462.
- Kagan, I., Iyer, A., Lindner, A., and Andersen, R.A. (2010). Space representation for eye movements is more contralateral in monkeys than in humans. *Proc. Natl. Acad. Sci. USA* 107, 7933–7938.
- Kellis, S., Rieth, L., Baker, B., Bashford, L., Pejsa, K.W., Lee, B., Liu, C., and Andersen, R.A. (2019). Quantitative scanning electron microscopy analysis of intracortical microelectrode arrays after five years in human neocortex. Program No. 670.09/M23. In 2019 Neuroscience Meeting Planner (Chicago, IL: Society for Neuroscience).
- King, C.E., Wang, P.T., McCrimmon, C.M., Chou, C.C., Do, A.H., and Nenadic, Z. (2015). The feasibility of a brain-computer interface functional electrical stimulation system for the restoration of overground walking after paraplegia. *J. Neuroeng. Rehabil.* 12, 80.
- Macé, E., Montaldo, G., Cohen, I., Baulac, M., Fink, M., and Tanter, M. (2011). Functional ultrasound imaging of the brain. *Nat. Methods* 8, 662–664.

- Mace, E., Montaldo, G., Osmanski, B.-F., Cohen, I., Fink, M., and Tanter, M. (2013). Functional ultrasound imaging of the brain: theory and basic principles. *IEEE Trans. Ultrason. Ferroelectr. Freq. Control* *60*, 492–506.
- Maresca, D., Payen, T., Lee-Gosselin, A., Ling, B., Malounda, D., Demeñé, C., Tanter, M., and Shapiro, M.G. (2020). Acoustic biomolecules enhance hemodynamic functional ultrasound imaging of neural activity. *Neuroimage* *209*, 116467.
- Montaldo, G., Tanter, M., Bercoff, J., Benech, N., and Fink, M. (2009). Coherent plane-wave compounding for very high frame rate ultrasonography and transient elastography. *IEEE Trans. Ultrason. Ferroelectr. Freq. Control* *56*, 489–506.
- Musallam, S., Corneil, B.D., Greger, B., Scherberger, H., and Andersen, R.A. (2004). Cognitive control signals for neural prosthetics. *Science* *305*, 258–262.
- Norman, S.L., McFarland, D.J., Miner, A., Cramer, S.C., Wolbrecht, E.T., Wolpaw, J.R., and Reinkensmeyer, D.J. (2018). Controlling pre-movement sensorimotor rhythm can improve finger extension after stroke. *J. Neural Eng.* *15*, 056026.
- Nowlis, D.P., and Kamiya, J. (1970). The control of electroencephalographic alpha rhythms through auditory feedback and the associated mental activity. *Psychophysiology* *6*, 476–484.
- Osmanski, B.-F., Martin, C., Montaldo, G., Lanièce, P., Pain, F., Tanter, M., and Gurden, H. (2014). Functional ultrasound imaging reveals different odor-evoked patterns of vascular activity in the main olfactory bulb and the anterior piriform cortex. *Neuroimage* *95*, 176–184.
- Pandya, D.N., and Seltzer, B. (1982). Intrinsic connections and architectonics of posterior parietal cortex in the rhesus monkey. *J. Comp. Neurol.* *204*, 196–210.
- Peirce, J.W. (2009). Generating stimuli for neuroscience using PsychoPy. *Front. Neuroinform.* *2*, 10.
- Pnevmatikakis, E.A., and Giovannucci, A. (2017). NoRMCorre: An online algorithm for piecewise rigid motion correction of calcium imaging data. *J. Neurosci. Methods* *297*, 83–94.
- Polikov, V.S., Tresco, P.A., and Reichert, W.M. (2005). Response of brain tissue to chronically implanted neural electrodes. *J. Neurosci. Methods* *148*, 1–18.
- Quiñ Quiroga, R., Snyder, L.H., Batista, A.P., Cui, H., and Andersen, R.A. (2006). Movement intention is better predicted than attention in the posterior parietal cortex. *J. Neurosci.* *26*, 3615–3620.
- Rabut, C., Correia, M., Finel, V., Pezet, S., Pernot, M., Deffieux, T., and Tanter, M. (2019). 4D functional ultrasound imaging of whole-brain activity in rodents. *Nat. Methods* *16*, 994–997.
- Rabut, C., Yoo, S., Hurt, R.C., Jin, Z., Li, H., Guo, H., Ling, B., and Shapiro, M.G. (2020). Ultrasound Technologies for Imaging and Modulating Neural Activity. *Neuron* *108*, 93–110.
- Rau, R., Kruijzinga, P., Mastik, F., Belau, M., de Jong, N., Bosch, J.G., Scheffer, W., and Maret, G. (2018). 3D functional ultrasound imaging of pigeons. *Neuroimage* *183*, 469–477.
- Rungta, R.L., Chaigneau, E., Osmanski, B.-F., and Charpak, S. (2018). Vascular compartmentalization of functional hyperemia from the synapse to the pia. *Neuron* *99*, 362–375.e4.
- Sakellaridi, S., Christopoulos, V.N., Aflalo, T., Pejsa, K.W., Rosario, E.R., Ouellette, D., Pouratian, N., and Andersen, R.A. (2019). Intrinsic Variable Learning for Brain-Machine Interface Control by Human Anterior Intraparietal Cortex. *Neuron* *102*, 694–705.e3.
- Sauvage, J., Flesch, M., Férin, G., Nguyen-Dinh, A., Porée, J., Tanter, M., Pernot, M., and Deffieux, T. (2018). A large aperture row column addressed probe for in vivo 4D ultrafast doppler ultrasound imaging. *Phys. Med. Biol.* *63*, 215012.
- Shanechi, M.M. (2019). Brain-machine interfaces from motor to mood. *Nat. Neurosci.* *22*, 1554–1564.
- Shimoda, K., Nagasaka, Y., Chao, Z.C., and Fujii, N. (2012). Decoding continuous three-dimensional hand trajectories from epidural electrocorticographic signals in Japanese macaques. *J. Neural Eng.* *9*, 036015.
- Sieu, L.-A., Bergel, A., Tiran, E., Deffieux, T., Pernot, M., Gennisson, J.-L., Tanter, M., and Cohen, I. (2015). EEG and functional ultrasound imaging in mobile rats. *Nat. Methods* *12*, 831–834.
- Snyder, L.H., Batista, A.P., and Andersen, R.A. (1997). Coding of intention in the posterior parietal cortex. *Nature* *386*, 167–170.
- Snyder, L.H., Batista, A.P., and Andersen, R.A. (2000). Intention-related activity in the posterior parietal cortex: a review. *Vision Res.* *40*, 1433–1441.
- Soloukey, S., Vincent, A.J.P.E., Satoe, D.D., Mastik, F., Smits, M., Dirven, C.M.F., Strydis, C., Bosch, J.G., van der Steen, A.F.W., De Zeeuw, C.I., et al. (2020). Functional Ultrasound (fUS) During Awake Brain Surgery: The Clinical Potential of Intra-Operative Functional and Vascular Brain Mapping. *Front. Neurosci.* *13*, 1384.
- Thier, P., and Andersen, R.A. (1996). Electrical microstimulation suggests two different forms of representation of head-centered space in the intraparietal sulcus of rhesus monkeys. *Proc. Natl. Acad. Sci. USA* *93*, 4962–4967.
- Thier, P., and Andersen, R.A. (1998). Electrical microstimulation distinguishes distinct saccade-related areas in the posterior parietal cortex. *J. Neurophysiol.* *80*, 1713–1735.
- Urban, A., Dussaux, C., Martel, G., Brunner, C., Mace, E., and Montaldo, G. (2015). Real-time imaging of brain activity in freely moving rats using functional ultrasound. *Nat. Methods* *12*, 873–878.
- Wang, P.T., King, C.E., Chui, L.A., Do, A.H., and Nenadic, Z. (2012). Self-paced brain-computer interface control of ambulation in a virtual reality environment. *J. Neural Eng.* *9*, 056016.
- Wang, P.T., Camacho, E., Wang, M., Li, Y., Shaw, S.J., Armacost, M., Gong, H., Kramer, D., Lee, B., Andersen, R.A., et al. (2019). A benchtop system to assess the feasibility of a fully independent and implantable brain-machine interface. *J. Neural Eng.* *16*, 066043.
- Welle, C.G., Gao, Y.-R., Ye, M., Lozzi, A., Boretsky, A., Abliz, E., and Hammer, D.X. (2020). Longitudinal neural and vascular structural dynamics produced by chronic microelectrode implantation. *Biomaterials* *238*, 119831.
- Wilke, M., Kagan, I., and Andersen, R.A. (2012). Functional imaging reveals rapid reorganization of cortical activity after parietal inactivation in monkeys. *Proc. Natl. Acad. Sci. USA* *109*, 8274–8279.
- Wolpaw, J.R., and McFarland, D.J. (2004). Control of a two-dimensional movement signal by a noninvasive brain-computer interface in humans. *Proc. Natl. Acad. Sci. USA* *101*, 17849–17854.
- Wolpaw, J.R., McFarland, D.J., Neat, G.W., and Forneris, C.A. (1991). An EEG-based brain-computer interface for cursor control. *Electroencephalogr. Clin. Neurophysiol.* *78*, 252–259.
- Woolley, A.J., Desai, H.A., and Otto, K.J. (2013). Chronic intracortical microelectrode arrays induce non-uniform, depth-related tissue responses. *J. Neural Eng.* *10*, 026007.

STAR★METHODS

KEY RESOURCES TABLE

REAGENT or RESOURCE	SOURCE	IDENTIFIER
Software and algorithms		
MATLAB 2020a	Mathworks	RRID:SCR_001622
Python Programming Language v2.7	Python Software Foundation	RRID:SCR_008394
PsychoPy v3.1.5	https://github.com/psychoopy/psychoopy	RRID:SCR_006571
Other		
Vantage 128 Research Ultrasound System	Verasonics	N/A
DOMINO linear array probe	Vernon	H.S.#901812000

RESOURCE AVAILABILITY

Lead contact

Further information and requests for resources should be directed to and will be fulfilled by the Lead Contact, Richard A. Andersen (richard.andersen@vis.caltech.edu).

Materials availability

This study did not generate new unique materials.

Data and code availability

Data and analysis software to replicate the primary results will be shared upon request from Sumner Norman (sumnern@caltech.edu).

EXPERIMENTAL MODEL AND SUBJECT DETAILS

We implanted two healthy adult male rhesus macaques (*Macaca mulatta*) weighing 10–13 kg. All surgical and animal care procedures were done in accordance with the National Institutes of Health Guide for the Care and Use of Laboratory Animals and were approved by the California Institute of Technology Institutional Animal Care and Use Committee.

METHOD DETAILS

Animal preparation and implant

We implanted two animals with polyether ether ketone head caps anchored to the skull with titanium screws. We then placed a custom polyether ketone (Monkey H) or stainless-steel (Monkey L) head holder on the midline anterior aspect of the cap. Finally, we placed a unilateral square chamber of 2.4 cm inner diameter, made of polyetherimide (Monkey H) or nylon (Monkey L) over a craniotomy above the left intraparietal sulcus. The dura underneath the craniotomy was left intact. To guide the placement of the chamber, we acquired high-resolution (700 μm) anatomical MRI images before the surgery using a Siemens 3T MR scanner, with fiducial markers to register the animals' brains to stereotaxic coordinates.

Behavioral setup

During each recording session, the monkeys were placed in a dark anechoic room. They sat in a custom designed primate chair, head fixed, facing an LCD monitor ~30 cm away. Visual stimuli were presented using custom Python software based on PsychoPy (Peirce, 2009). Eye position was monitored at 60 Hz using a miniature infrared camera (Resonance Technology, Northridge, CA, USA) and ViewPoint pupil-tracking software (Arrington Research, Scottsdale, AZ, USA). Reaches were performed using a 2-dimensional joystick (Measurement Systems). Both eye and cursor positions were recorded simultaneously with the stimulus and timing information and stored for offline access. Data analysis was performed in MATLAB 2020a (MathWorks, Natick, MA, USA) using standard desktop computers.

Behavioral tasks

The animals performed memory-guided eye movements to peripheral targets (Figure 2A). Each trial started with a fixation cue (red diamond; 1.5 cm side length) presented in the center of screen (fixation period). The animal fixated for 5.35–6.33 s depending on

training (mean 5.74 s across sessions). Then, a single cue (red diamond; 1.5 cm side length) appeared either on the left or the right hemifield for 200 ms, indicating the location of the target. Both targets were located equidistantly from the central fixation cue (23° eccentricity). After the cue offset, the animals were required to remember the location of the targets while maintaining eye fixation (memory period). This period was chosen to be sufficiently long to capture hemodynamic transients. The memory period was consistent within each session but varied across sessions from 4.02–5.08 s (mean 4.43 s across session) depending on the animal's level of training. Once the central fixation cue disappeared (i.e., go signal) the animals performed a direct eye movement (saccade) within 500 ms to the remembered location of the target. If the eye position arrived within a radius of 5° of the targets, it was re-illuminated and stayed on for the duration of the hold period (1 s). If the animal broke eye fixation before the go signal (i.e., shifted their gaze outside of a window of 7.5 cm, corresponding to 14° of visual angle) the trial was aborted. Successful trials were followed by a liquid reward. The fixation and memory periods were subject to 400 ms of jitter sampled from a uniform distribution to preclude the animal from anticipating the change(s) of the trial phase.

Both animals also performed memory-guided reach movements to peripheral targets using a 2-dimensional joystick positioned in front of the chair with the handle at knee level. Each trial started with two fixation cues presented at the center of the screen. The animal fixated his eyes on the red diamond cue (1.5 cm side length) and acquired the green cue by moving a square cursor (0.3 cm side length) controlled by his right hand on the joystick (fixation period). The animal fixated for 2.53–5.85 s depending on training (mean 3.94 s across sessions). Then, a single green target (1.5 cm side length) was presented either on the left or the right visual field for a short period of time (300 ms). After the cue offset, the animal was required to remember the location of the targets for a memory period while maintaining eye and hand fixation. The memory period was consistent within each session but varied across sessions from 3.23–5.20 (mean 4.25 s across session). Once the central green cue disappeared, the animal performed a direct reach to the remembered target location within 500 ms, without breaking eye fixation. If they moved the cursor to the correct goal location, the target was re-illuminated and stayed on for duration of the hold period (1 s). Targets were placed at the same locations as in saccade trials. If the cursor moved out of the target location, the target was extinguished, and the trial was aborted. Any trial in which the animal broke eye fixation or initiated a reaching movement before the go signal or failed to arrive at the target location was aborted. Successful trials were followed with the same liquid reward as in saccade trials. The fixation and memory periods were subject to 400 ms of jitter sampled from a uniform distribution to preclude the animal from anticipating the change(s) of the trial phase.

We also trained both animals on a task that intermingled memory delayed saccades and reaches (Figure 5A). Similar to the reach task, each trial started with two fixation cues presented at the center of the screen: one for his eyes and one for his right hand. The target sizes were maintained from the reach task. The key difference was that the color of the gaze fixation diamond was randomized as blue or red: blue to cue saccades and red to cue reaches. After a 4.3 s memory period, a single white target (1.5 cm side length) was presented either on the left or right visual field for a short period of time (300 ms). After the cue offset, the animal was required to remember the location of the targets for the duration of the memory period. The memory period across all sessions for both monkeys was 4.0 s. Once the central green cue disappeared, the animal performed a saccade or reach via joystick to the remembered target location within 500 ms, without breaking fixation of the non-cued effector. If they moved the cursor to the correct goal location, the target was re-illuminated and stayed on for the duration of the hold period (1 s). If the cued effector moved out of the target location, the target was extinguished, and the trial was aborted. Any trial in which the animal broke fixation of the non-cued effector or initiated a movement of the cued effector before the go signal or failed to arrive at the target location was aborted. Successful trials were followed with the same liquid reward as in saccade and reach trials. The fixation and memory periods were subject to 400 ms of jitter sampled from a uniform distribution to preclude the animal from anticipating the change(s) of the trial phase.

Functional ultrasound sequence and recording

During each recording session, we placed the ultrasound probe (128 elements linear array probe, 15.6 MHz center frequency, 0.1 mm pitch, Vermon, France) in the chamber with acoustic coupling gel. This enabled us to acquire images from the posterior parietal cortex (PPC) with an aperture of 12.8 mm and depths up to 23 mm (results presented here show up to 16 mm depth). This large field of view allowed us to image several PPC regions simultaneously. These superficial and deep cortical regions included, but were not limited to, area 5d, lateral intraparietal (LIP) area, medial intraparietal (MIP) area, medial parietal area (MP), and ventral intraparietal (VIP) area.

We used a programmable high-framerate ultrasound scanner (Vantage 128 by Verasonics, Kirkland, WA) to drive a 128-element 15 MHz probe and collect the pulse echo radiofrequency data. We used a plane-wave imaging sequence at a pulse repetition frequency of 7500 Hz. We transmitted plane waves at tilted angles of –6 to 6° in 3° increments. We then compounded data originating from each angle to obtain one high-contrast B-mode ultrasound image (Mace et al., 2013). Each high-contrast B-mode image was formed in 2 ms, i.e., at a 500 Hz framerate.

Regional changes in cerebral blood volume induced by neurovascular coupling can be captured by ultrafast power Doppler ultrasound imaging (Macé et al., 2011). We implemented an ultrafast power Doppler sequence using a spatiotemporal clutter-filter to separate blood echoes from tissue backscattering. We formed Power Doppler images of the NHP brain using 250 compounded B-mode images collected over 0.5 s. Image formation and data storage were performed after the pulse sequence and took ~0.5 s. Thus, the pulse sequence and image formation/save resulted in power Doppler functional mapping of the NHP brain at a 1 Hz refresh rate.

Anatomical PPC regions were spatially located by their stereotaxic positions from the pre-surgical MRI. Response of these functional areas was confirmed by mapping activated voxels obtained during the experimental phase of this work. If necessary,

the imaging plane was adjusted to record the most responsive area. Each acquisition consisted of 900–3600 blocks of 250 frames where each block represented 1 s of data (equivalent to 15–60 minutes runtime). Finally, we stored the in-phase and quadrature sampled data to high-speed solid-state drive memory for offline processing.

Power Doppler image processing

We used singular value decomposition to discriminate red blood cell motion from tissue motion and extracted the Doppler signal in each ensemble of 250 coherently compounded frames (Demené et al., 2015; Montaldo et al., 2009). The resulting images were then stored in a 3D array of 2D images in time series. In some experiments, we observed motion of the entire imaging frame. These shifts were indicative of a change in the position of the probe/tissue interface due to uncommonly forceful movements of the animal. We corrected for these events using rigid-body image registration based on the open source NoRMCorre package (Pneumatikakis and Giovannucci, 2017), using an empirical template created from the first 20 frames from the same session. We also tested nonrigid image registration but found little improvement, confirming that motion observed was due to small movements between the probe/dura interface rather than changes in temperature or brain morphology.

QUANTIFICATION AND STATISTICAL ANALYSIS

All analyses were performed using MATLAB 2020a.

ERA waveforms and statistical parametric maps

We display event-related average (ERA) waveforms (Figures 2C–2F, 2H, 2I, 3C, 3D, 3F, and 3G) of power Doppler change as percentage change from baseline. The baseline consists of the three seconds preceding the first Doppler image obtained after the directional cue was given on any given trial. ERA waveforms are represented as a solid line with surrounding shaded areas representing the mean and standard deviation. We generated activation maps (Figures 2B, 2G, 3B, and 3E) by performing a one-sided t test for each voxel individually with false discovery rate (FDR) correction based on the number of voxels tested. In this test, we compared the area under the curve of the change in power Doppler during the memory phase of the event-related response. The movement direction represented the two conditions to be compared, and each trial represented one sample for each condition. We chose a one-sided test because our hypothesis was that contralateral movement planning would elicit greater hemodynamic responses in LIP compared to ipsilateral planning (based on canonical LIP function). This has the added benefit of being easily interpretable: areas of activation represent contralateral tuning. Voxels with values of $p < 0.01$ are displayed as a heatmap overlaid on a background vascular map for anatomical reference.

Single trial decoding

Decoding single trial movement intention involved three parts: 1) aligning CBV image time series with behavioral labels, 2) feature selection, dimensionality reduction and class discrimination, and 3) cross validation and performance evaluation (Figure 4A). First, we divided the imaging dataset into event aligned responses for each trial, i.e., 2D Power Doppler images through time for each trial. We then separated trials into a training set and testing set according to a 10-fold cross validation scheme. The training set was attached to class labels that represented the behavioral variable being decoded. For example, movement direction would be labeled left or right. The test set was stripped of such labels. Features were selected in the training set by ranking each voxel's q-value comparing the memory phase responses to target direction in the training data. Direction-tuned voxels (FDR corrected for number of pixels in image, $q < 0.05$) of up to 10% of the total image were kept as features. We also tested selecting features by drawing regions of interest around relevant anatomical structures e.g., LIP. Although this method can outperform q-maps, it is more laborious and depends on user skill, so we do not present its results here. For the intermingled effector task, we used all features (i.e., the whole image) because it did not require combining multiple t-maps. For dimensionality reduction and class separation, we used classwise principal component analysis (CPCA) and linear discriminant analysis (LDA) (Das and Nenadic, 2009), respectively. This decoding method has been implemented with success in many real-time BMIs (Do et al., 2013, 2011; King et al., 2015; Wang et al., 2019, 2012), and is especially useful in applications with high dimensionality. CPCA computes the principal components (PCs) in a piecewise manner individually for training data of each class. We retained principal components to account for > 95% of variance. We improved class separability by running linear discriminant analysis (LDA) on the CPCA-transformed data. Mathematically the transformed feature for each trial can be represented by $f = T_{LDA} \Phi_{CPCA}(d)$, where $d \in \mathbb{R}^1$ are the flattened imaging data for a single trial, Φ_{CPCA} is the piecewise linear CPCA transformation, and T_{LDA} is the LDA transformation. Φ_{CPCA} is physically related to space and time and thus can be viewed within the context of physiological meaning (Figure 4E). We subsequently used Bayes rule to calculate the posterior probabilities of each class given the observed feature space. Because CPCA is a piecewise function, this is done twice, once for each class, resulting in four posterior likelihoods: $P_L(L|f^*)$, $P_L(R|f^*)$, $P_R(L|f^*)$, $P_R(R|f^*)$, where f^* represents the observation, P_L and P_R represent the posterior probabilities in the CPCA subspaces created with training data from left-directed and right-directed trials, respectively. Finally, we store the optimal PC vectors and corresponding discriminant hyperplane from the subspace with the highest posterior probability. We then used these findings to predict the behavioral variable of interest for each trial in the testing set. That is, we compute f^* from fUS imaging data for each trial in the testing set to predict the upcoming movement direction. Finally, we rotate the training and testing sets according to k-fold validation, storing the BMI performance metrics for each iteration. We report the mean decoding accuracy as a percentage of correctly predicted trials (Figure 4B). In measures across

multiple sessions where an independent variable is being tested (e.g., number of trials in training set), we use a normalized accuracy that is linearly scaled to [0, 1] where 0 is chance level (50%) and 1 is the maximum accuracy across the set of values used in the independent variable (e.g., Figure 4C). This was necessary to regularize raw accuracy values across multiple sessions and animals.

Analysis of training set sample size

As BMI models increase in complexity, their need for data also increases. To demonstrate the robustness of our piecewise linear decoding scheme to limited data, we systematically reduced the amount of data used in the training set (Figure 4C). We used $N-i$ trials in the training set and i trials in the testing set in a cross-validated manner, rotating the training/testing set i times for $i = 1, 2, \dots, N-10$. We stop at $N-10$ because accuracy was diminished to chance level and when less than 10 trials are used in the training set, it becomes increasingly likely that there will be an under- or non-represented class, i.e., few or no trials to one of the movement directions. We report the mean normalized accuracy standard error of the means (SEM) across both animals and all recording sessions as a function of the number of trials in the training set ($N-i$) (Figure 4C).

Multicoder for intermingled effectors task

For the intermingled effectors task (Figure 5), we used the same decoding scheme described above to decode effector and direction. However, instead of using data from the period defined by the experiment, we used a decision tree to define the task period. That is, we first predicted the memory period from the non-memory periods (i.e., task epoch versus no-task epoch). To do this, we labeled each frame of fUS in the training set with a label for task or no-task. We then decoded each frame in the testing set using the same decoding scheme described above. The primary difference of note here is that we used individual frames of data rather than cumulative frames from within a known task period. We then refined these predictions by assuming that any time the classifier predicted the animal had entered a task state, they would be in that task state for three seconds. This allowed us to use three seconds' worth of data to train and decode the effector and direction variables. Note that while the task/no-task classifier makes a prediction every 1 s, the effector and direction make a prediction for each trial defined by the task/no-task classifier.

Cross temporal decoding

We also performed an analysis to determine the nature of hemodynamic encoding in PPC using a cross-temporal decoding technique. In this analysis, we used all temporal combinations of training and testing data, using a one second sliding window. We used 1 s of data from all trials to train the decoder and then attempted to decode from each of the 1 s windows of testing data throughout the trial. We then updated the training window and repeated the process. This analysis results in an $n \times n$ array of accuracy values where n is the number of time windows in the trial. We report the 10-fold cross-validated accuracies as a percentage of correctly predicted trials (Figure 4D). To assess the statistical significance of these results, we used a Bonferroni corrected binomial test versus chance level (0.5) where the number of comparisons was n^2 . We overlaid a contour at $p = 0.05$ to indicate the temporal boundaries of significant decoding accuracies.

Decoding with reduced spatial resolution

Part of the motivation for using fUS is its spatial resolution. To test the effects of increased resolution, we synthetically reduced the resolution of the in-plane imaging data using a Gaussian filter. We performed this analysis at all combinations of x and z direction (width and depth, respectively) starting at true resolution (i.e., 100 μm) up to a worst-case of 5 mm resolution. We report the 10-fold cross-validated accuracy values as a function of these decreasing resolutions as a 2D heatmap and as 1D curves of mean accuracy in both the x and z directions with shaded areas representing s.e.m. (Figure 6A). A limitation of this approach is that we cannot downsample the out-of-plane dimension. Thus, the reported accuracy values are likely higher than those attainable by a technique with isotropic voxel size, e.g., fMRI.

Decoding with different time windows

To analyze the effect of cumulative versus fixed length decoders, we used different sliding windows of data (1 s, 2 s, 3 s) to decode upcoming movement direction (left or right) using data from the memory delay period. We report these results using accuracy as a function of trial time and the maximum accuracy achieved during the memory period for each session (Figure 6B). Accuracies are represented at each time point through the fixation and memory periods using data aligned to the end of the time bin used for decoding. For example, an accuracy at $t = 3$ s for a decoder using 3 s of data represents a result trained on data from $t = 0-3$ s. To assess significance between different conditions, we used a student's two-tailed t test.

Power Doppler quantiles

We also investigated the source of hemodynamic information content by segmenting the images according to their mean power Doppler signal as a proxy for mean cerebral blood flow within a given area. Specifically, we segmented the image into deciles by mean power Doppler signal within a session, where higher deciles represented higher power and thus higher mean blood flow (Figure 6C). Deciles were delineated by the number of voxels, i.e., the number of voxels was the same within each segment and did not overlap. Using only the voxels within each decile segment, we computed the mean accuracy for each recording session. We report the mean normalized accuracy across all recording sessions (Figure 4C) where shaded error bars represent SEM.